

Microstructure Evolution of a Multimodal Gamma-Prime Ni-Based Superalloy Characterized by *In Situ* Diffraction



MUHAMMAD AWAIS, WILLIAM R. HIXSON, QUINTON VICTOR, CALLAHAN O'NEAL, JAN ILAVSKY, and JAMES COAKLEY

The relationship between the evolution of microstructure, deformation micromechanisms and mechanical properties is difficult to establish in multimodal size distribution γ' superalloys, as the microstructure evolves with both temperature and time, and multiple strengthening mechanisms across each size distribution contribute to mechanical performance. *In situ* X-ray scattering can offer unparalleled insight regarding microstructure evolution at the temperatures and stresses of importance to gas-turbine applications; however, *in situ* X-ray diffraction has not been applied to the study of multimodal γ' distribution superalloys. Herein, lattice parameter evolution of secondary and tertiary γ' precipitates in a representative superalloy, Nimonic 115, is determined between 750 °C and 950 °C and correlated to room-temperature SEM and microhardness values. A large positive lattice parameter misfit of secondary γ' induces precipitate splitting, and the tertiary γ' goes into dissolution at \sim 800 °C, but with little apparent change in hardness values. The volume fraction of γ' decreases above 900 °C and precipitate-matrix coherency is lost, and there is a corresponding decrease in microhardness values. The diffraction analysis demonstrates the capability to determine critical microstructural parameters of both precipitate size distributions *in situ*, representing an additional tool for determining microstructure-mechanical property relationships of multimodal superalloys.

<https://doi.org/10.1007/s11661-023-07013-z>

© The Minerals, Metals & Materials Society and ASM International 2023

I. INTRODUCTION

THE exceptional high temperature properties of Ni-based superalloys are based on synergistic contributions from two phases, where a disordered A1 fcc matrix (γ , Figure 6) provides ductility, but deformation is hindered by the ordered fcc L1₂ intermetallic precipitates (γ'), thereby achieving high strength. Aerospace disk alloys that operate at intermediate temperatures up to \sim 750 °C (such as RR1000,¹ René 88DT² and René 95³) are processed to obtain multimodal γ' precipitate size distributions, where the microstructure and properties are dependent on the thermal processing conditions. A thermal aging processing step coarsens a secondary γ' precipitate distribution typically \sim 200 nm diameter, and

a tertiary precipitate size distribution \sim 10 nm diameter nucleates on rapid cooling from the aging temperature.^{1–6}

It has been suggested that differences of nearly two orders of magnitude in crack growth rates can be attributed to the evolution of the tertiary γ' size distribution.^{1,7} However, isolating the contribution of tertiary and secondary γ' precipitates to mechanical properties remains challenging when one considers (i) the multiple strengthening mechanisms that contribute to superalloy mechanical properties,^{8,9} (ii) that the mechanisms of microstructure evolution across temperatures and time within multimodal γ' superalloys are not fully understood,⁴ (iii) quantifying precipitate evolution at the atomic and nanoscale is non-trivial, and (iv) room-temperature characterization may not be representative of the microstructure under the temperatures of relevance for engine applications. Thus, the characterization of multimodal γ' microstructure evolution under laboratory conditions that reflect service conditions is critical.

In situ neutron and X-ray scattering techniques can provide unparalleled insight regarding microstructure evolution^{10–18} and deformation micromechanics^{19–29} at the elevated temperatures and stresses of importance for

MUHAMMAD AWAIS, WILLIAM R. HIXSON, QUINTON VICTOR, CALLAHAN O'NEAL, and JAMES COAKLEY are with the Department of Mechanical and Aerospace Engineering, University of Miami, Coral Gables, FL 33146. Contact e-mail: jcoakley@miami.edu JAN ILAVSKY is with the Advanced Photon Source, Argonne National Laboratory, Lemont, IL 60439.

Manuscript submitted June 28, 2022; accepted February 9, 2023.

Article published online March 2, 2023

superalloy applications. However, to the authors' knowledge, *in situ* diffraction has not been applied to the study of multimodal precipitate size distribution evolution. Herein, microstructure evolution of the ~60 pct γ' volume fraction⁴ multimodal superalloy Nimonic 115 (Ni 115) during thermal holds and cooling is presented, supported with *ex situ* scanning electron microscopy and correlated to hardness testing.

It is demonstrated, for the first time, that the microstructure evolution of both precipitate size distributions can be distinguished by *in situ* diffraction techniques, that the lattice evolution is initially anisotropic which may be related to residual strains, and that mechanical properties diminish following thermal exposure at 900–950 °C associated with a loss in precipitate–matrix coherency and γ' volume fraction.

II. EXPERIMENTAL DETAILS

A. X-ray Scattering and Peak Fitting

Samples were prepared from a forged bar of Ni 115⁴ that had received a typical industry standard supersolvus solution heat treated at 1190 °C for 1.5 hours, air-cooled, then aged at 1100 °C for 6 hours and air-cooled again. This produces a microstructure containing very limited primary γ' , such that the alloy can be considered a bimodal distribution of secondary and tertiary γ' precipitates.^{4,30} The alloy composition was measured with inductively coupled plasma–optical emission spectrometry and LECO gas analyzers, Table I.

50 μm thickness foils were prepared from the bar via sectioning and mechanical grinding. The foils were mounted in a Linkam 1500 heating stage and placed in the 9-ID beamline at the Advanced Photon Source (APS) for measurements at 21 keV photon energy and 0.8 x 0.2 mm beam size. The average grain size is approximately 20–30 microns determined from microscopy analysis, thus scattering should arise from approximately 500 grains. *in situ* X-ray diffraction (XRD) measurements were recorded with count times of 30 seconds per measurement during the thermal procedure presented in Figure 1. The detector covers an azimuthal angle of approximately 40 °C at the (100) reflection and 20 °C at the (111) reflection.

A representative XRD profile is shown in Figure 2 with the corresponding phase peak positions identified. Minor reflections corresponding to a TiC-based carbide ($Fm\bar{3}m$, [225] space group) are also apparent in the spectrum.³¹ Individual diffraction peaks were fitted by pseudo-Voigt peak fitting routines in Wavemetrics

IGOR Pro software, with fitting parameters of background, intensity, width, shape, and peak position. The γ' reflections were fitted by two pseudo-Voigt peaks up to ~800–825 °C, Figures 3(a) and 4, with the constraints of a single peak shape and width for both peaks. Above these temperatures, the γ' reflections are fitted by a single pseudo-Voigt peak fitting routine to data, Figure 3.

Accurate deconvolution of the $\gamma + \gamma'$ reflections is challenging when the lattice parameters of both phases are similar and therefore the lattice parameter mismatch $\delta = (a_{\gamma'} - a_{\gamma})/2((a_{\gamma'} + a_{\gamma}))$ is small, where a_x is the lattice parameter of phase x . One data analysis approach has been to constrain the (200) γ' peak position based on the fitting parameters of the (100) or (300) γ' peaks, for example.²¹ In the current data, the (300) peak intensity is initially low and decreases through the experiment [Figure 4(c)], and the γ' peak widths are narrow for the instrument resolution such that peak fitting is being

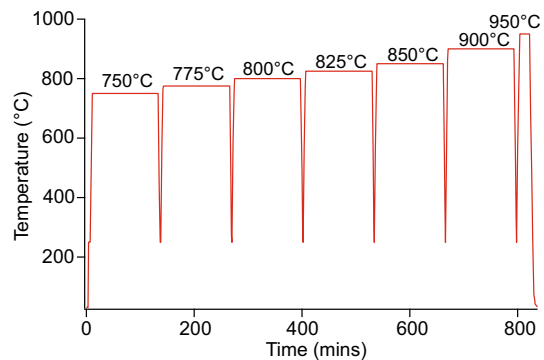


Fig. 1—Thermal cycle procedure of the *in situ* XRD measurements.

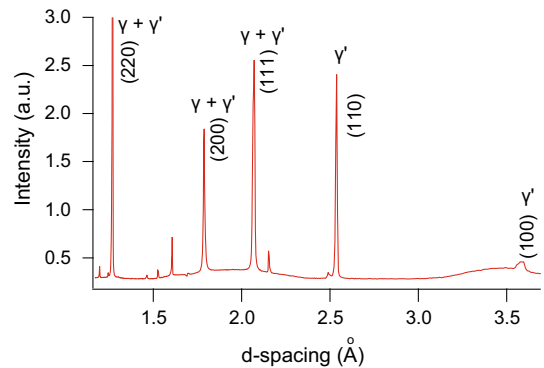


Fig. 2—Initial XRD pattern prior to heating. The intensity axis is cropped at 3.0 to illustrate the lower intensity superlattice reflections, where the (220) peak intensity is 12.6.

Table I. Ni 115 Composition Measured by Inductively Coupled Plasma Optical Emission Spectrometry (ICP-OES) and a LECO Carbon Sulfur (CS) Analyser

Element	Al	C	Cr	Co	Cu	Fe	Mo	Ni	Si	Ti	Zr
(Weight Percent)	4.85	0.15	15.0	15.2	0.2	0.4	3.64	Bal	0.003	3.96	0.042

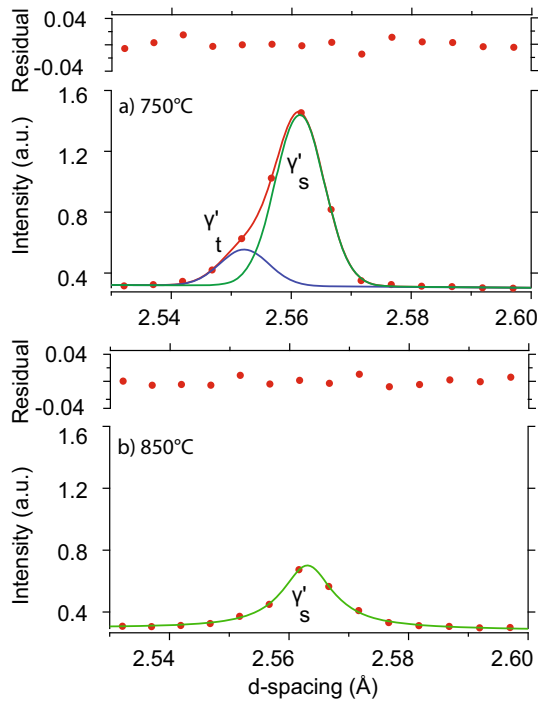


Fig. 3—Peak fitting routines applied to the (110) γ' reflection corresponding to (a) the start of the 750 °C and (b) 850 °C thermal holds (Fig. 1). γ'_s and γ'_t correspond to the secondary and tertiary γ' reflections, respectively.

performed to 3 - 5 data points for the (100) secondary γ' peak positions [Figure 4(a)]. The accurate constraining of the (200) γ' peak position from the (100) or (300) in order to deconvolute the (200) γ peak position is dependent on a highly accurate (100) or (300) peak fit, such that any noise in the (100) or (300) peak positions creates further noise in the deconvolution of the (200) γ peak position and the iterative fitting procedure becomes unreliable. Thus, we do not iteratively deduce the γ peak evolution for all measurements, but individually apply the fitting routine at low temperature (750 °C) and high temperature (950 °C) to deduce the γ peak positions, Figure 5. In these peak fits to (220) data, it is assumed that peak widths and shapes are equal and the intensity ratio of secondary to tertiary γ' is constrained from the (110) peak fits.

B. Microscopy & Hardness Testing

Samples were sequentially heat treated following the same heating procedure of the *in situ* X-ray diffraction (XRD) measurements, Figure 1, and air-cooled prior to microscopy. Room-temperature scanning electron microscopy (SEM) is presented in Figure 6 where the stated temperatures correspond to the temperature of the final thermal hold. Samples for SEM were prepared via mechanical grinding and polishing with a final polish using silica oxide polishing suspension (OPS). The γ phase was electrolytically etched at 2°V, 2°A for 1°s in a solution of 2 pct phosphoric acid diluted in distilled water. SEM was performed using a Zeiss Ultra Plus.

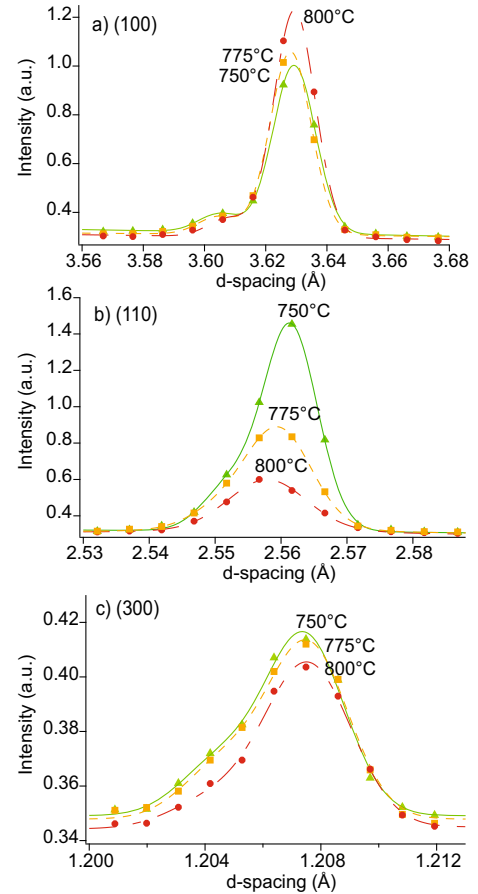


Fig. 4—(a) (100), (b) (110), and (c) (300) XRD and peak fits to data at the beginning of the 750 °C thermal hold and at the end of the 775 and 800 °C thermal holds (Fig. 1).

The SEM micrographs shown were analyzed using ImageJ software. Color threshold was applied to produce binary images of the γ and secondary γ' phases.⁴ Secondary γ' area fraction, precipitate number per unit area, and average precipitate size were calculated from thresholded image, from which equivalent precipitate diameter was calculated. The user dependency regarding a reasonable threshold value range and the determined area fraction, diameter, and number of precipitates per unit area was less than 10 pct, and so we approximate the error in this methodology as 10 pct.

Vickers microhardness tests were performed on the samples shown in Figure 6 utilizing a Wilson Tukon tester with a force of 200 gmf. Microhardness values were deduced from the indent size measured on a Keyence VHX microscope. 20 indents were made on each unetched sample surface to get a statistically relevant average hardness, and standard error was calculated for each condition.

III. RESULTS

A. In Situ X-ray Diffraction

The γ' reflections were noted to be spotty in the detector, associated with somewhat limited grain

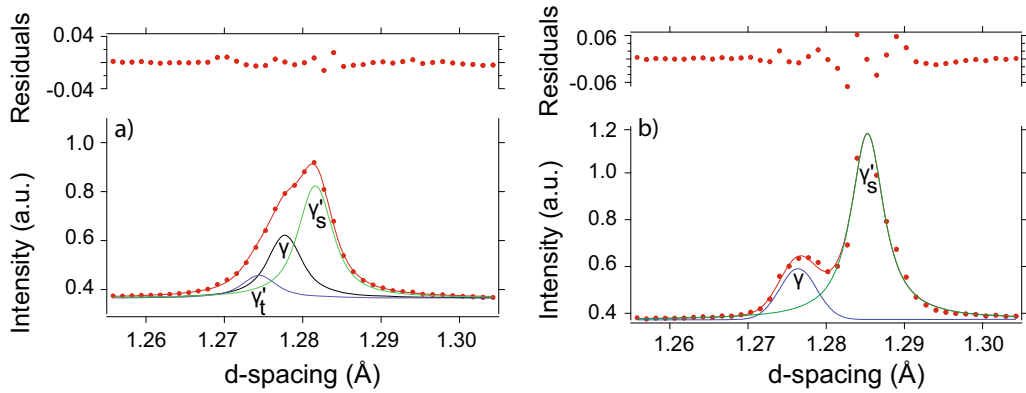


Fig. 5—Deconvolution of the γ , secondary γ'_s and tertiary $\gamma'_{t'}$ peak positions in the (220) reflections are shown at the end of (a) 750 °C and (b) 950 °C thermal holds.

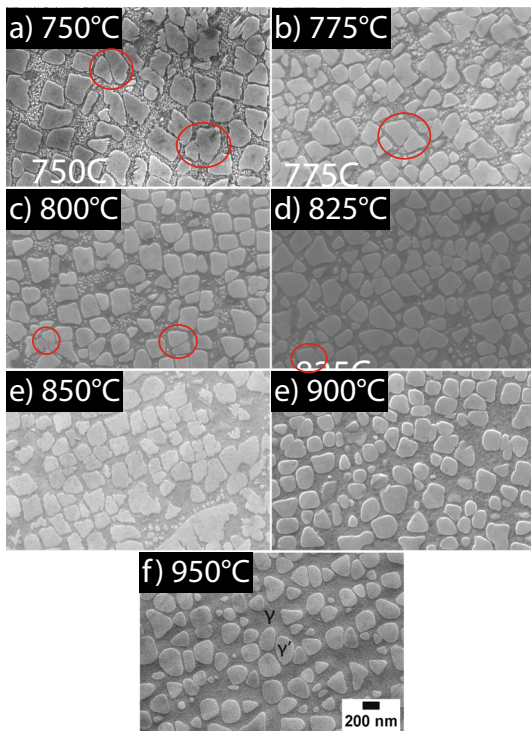


Fig. 6—Secondary electron SEM images of etched Ni 115 illustrating the microstructure evolution following each sequential thermal hold shown in Fig. 1. Evidence of γ' precipitate splitting is highlighted.

measurements and weak scattering intensity that arises from the γ' structure in superalloys. The $\gamma + \gamma'$ reflections appeared more uniform, where the γ phase typically produces greater intensity scattering in superalloys. A continuous ring was noted in the (111) reflection and partial rings in the (200) and (220) reflections. The data arising from the partial coverage of the 360 °C scattering are suitable for the analysis of the azimuthally averaged diffraction peak shape and, however, limit analysis regarding texture which requires full 2D detector coverage (where the strong (110) and (220) reflections in the initial diffraction pattern are likely due to texture, Figure 2).

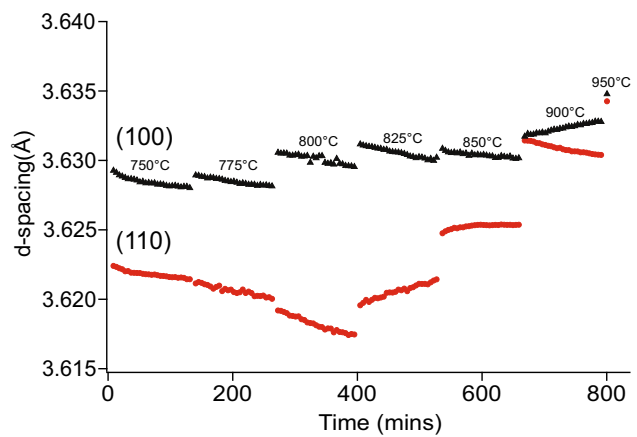


Fig. 7—Evolution of the secondary γ' lattice parameter with temperature and time when calculated from pseudo-Voigt peak fitting routines of the (100) and (110) XRD data.

The γ' peak fitting function shifts toward one peak from two peaks at ~ 800 °C, Figure 4. The lattice parameter of the secondary γ' deduced from the (100) and (110) peak fitting routines is presented in Figure 7. The difference in these calculated lattice parameter values and the response of the (110) d-spacing at 750–800 °C are discussed further in the subsequent section. The peak fits to the (110) data are provided in Figure 4(b) as visual confirmation that the (110) diffraction peak is shifting to lower d-spacing with increasing temperature. Above 800 °C, the d-spacing of both the (100) and (110) peaks increase with temperature steps, as expected, Figure 7.

B. SEM and Hardness Testing Results

The evolution of the secondary γ' area fraction, mean equivalent diameter, and particle number density (where it is assumed that the number of particles per unit area is equivalent to number density) calculated from SEM analysis of the sequential thermal exposures is presented in Figures 8(a) through (c). The room-temperature microhardness values are relatively constant (~ 490 – 515 Hv to the 900 °C sample), but decrease following the

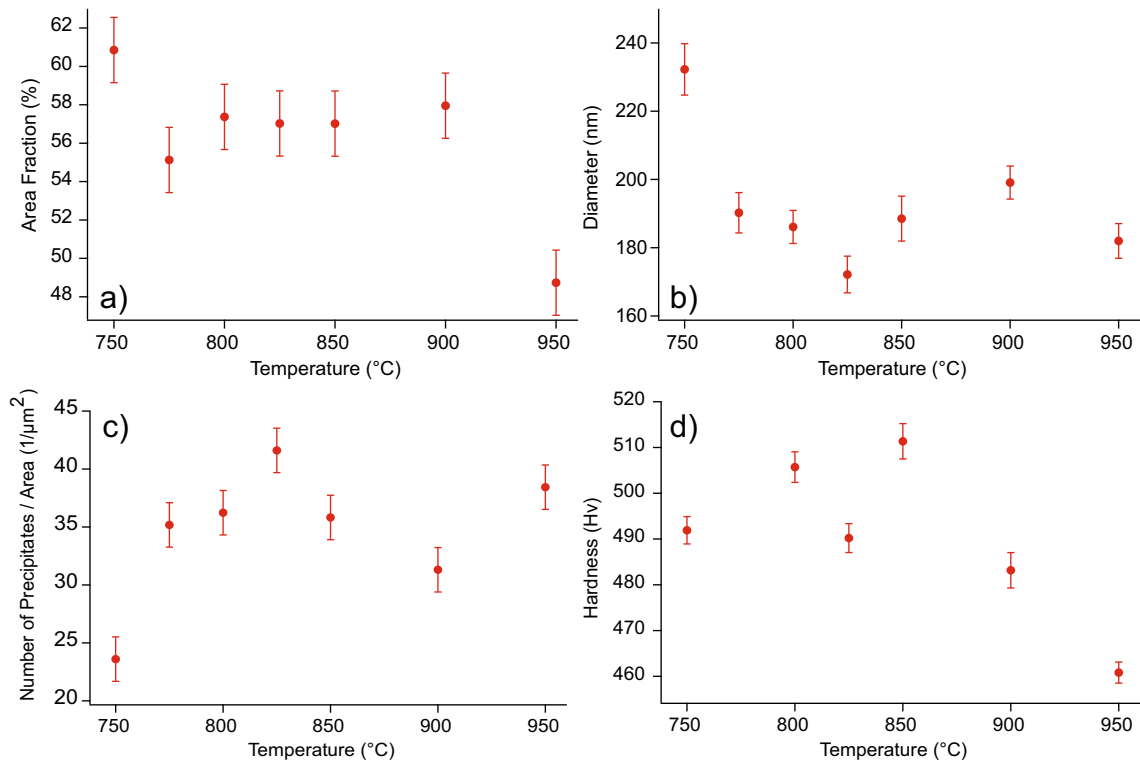


Fig. 8—Secondary γ' precipitate (a) area fraction, (b) equivalent mean diameter, and (c) number density deduced from room-temperature SEM image analysis following each sequential thermal hold. (d) Microhardness values determined from the same samples. The error range corresponds to the image threshold sensitivity on determined values for (a) through (c), and the statistical error from the distribution of hardness test results.

900–950 °C thermal exposure, Figure 8(d). These results are discussed in Section IV in light of the *in situ* XRD data and the archival literature regarding precipitate evolution theory and superalloy strengthening mechanisms.

IV. DISCUSSION

The secondary γ' area fraction across 750–900 °C thermal exposures is approximately constant at 58 ± 3 pct, Figure 8(a), with a maximum of ~ 61 pct at 750 °C. The removal of tertiary γ' following 800–825 °C thermal exposures observed in the SEM (Figure 6) does not correspond to an increase in secondary γ' area fraction, such that the tertiary γ' dissolution is due to the phase area fraction and composition adjusting to the new thermodynamic equilibrium at increased temperatures as opposed to fine precipitate dissolution associated with Ostwald ripening.

The mean equivalent diameter decreased from ~ 230 to ~ 190 nm following the first and second thermal holds, while the precipitate number density increased from ~ 24 to $\sim 35^\circ\mu\text{m}^{-2}$, Figures 8(b) and (c). This phenomenon is termed ‘reverse coarsening.’ There is extensive evidence of secondary γ' precipitate splitting highlighted in the micrographs of Figure 6, decreasing the mean equivalent precipitate diameter and increasing number density.^{32–39} Precipitate splitting appears to be a

dominant microstructure evolution mechanism in Ni 115 in the initial transient coarsening regime.⁴

Precipitate splitting is associated with large interface lattice parameter misfit inducing high elastic strain.³² The lattice parameter misfit with the secondary γ' at 750 °C is determined to be $\delta = 0.3$ pct in the (220) thus it is reasonable to suggest precipitate splitting as an initial precipitate evolution mechanism in this alloy system. Lifshitz Slyozov Wagner (LSW) based theories^{40,41} do not account for elastic strain energy and related effects on microstructure such as precipitate splitting.

It is difficult to determine the trends in the evolution of microstructural parameters determined from SEM analysis due to statistical scatter in the 775–900 °C thermal exposures, Figure 8. However, it can be concluded that the change in microstructure between 750 and 900 °C does not significantly affect microhardness. Comparing the microstructure following 750 and 900 °C thermal holds, the secondary γ' mean diameter decreased from ~ 230 to ~ 200 nm (-13 pct) and the number density has increased from ~ 23 to $\sim 32^\circ\mu\text{m}^{-2}$ ($+48$ pct) while hardness is relatively constant, Figure 8. Additionally, the tertiary γ' has gone into dissolution between 750 and 900 °C. If the hardness at 850 °C is regarded as a maximum, it represents a hardness increase of just 4 pct relative to the initial 750 °C measurement. Thus, we conclude that the tertiary γ' size distribution and secondary γ' precipitate splitting have minimal influence on overall

microhardness. Despite the fact that the number density of secondary γ' precipitates increases due to splitting, the original inter-particle distances between precipitates are not reduced, and this may explain the similar microhardness values.

The change in the γ' XRD peak shape as temperature is stepped represents the first successful application of *in situ* XRD to monitor two γ' size distributions, Figure 3. The correlation between the temperature at which the peak fitting routine shifts from doublet to singlet and the dissolution of the tertiary γ' observed in SEM is significant. The lattice parameter of secondary and tertiary γ' is expected to differ, given that they form at different temperatures and possess different compositions.³ Thus, these measurements suggest that phase evolution, phase transformations, and deformation micromechanisms of both size distributions could be deduced from *in situ* diffraction data in multimodal γ' superalloys, representing a broadening in the application of such techniques to superalloy metallurgy.

The constrained lattice parameter misfit at 750 °C is $\delta = 0.30 \text{ pct}$ for the secondary γ' and $\delta = -0.26 \text{ pct}$ for the tertiary γ' . To understand the difference in misfit between the two size distributions, the alloy thermal history and composition of each phase are considered. The final commercial heat-treatment step at 1100°C/6hours coarsens the secondary γ' distribution which may alter the precipitate/matrix interface coherency, after which the alloy is cooled and the tertiary γ' size distribution is nucleated. Thus, there may be a difference in the interface coherency. However, the authors' interpret this difference in misfit sign between size distributions as being associated with a difference in composition between secondary and tertiary γ' particles. Chen *et al.* determined that the Al content of the tertiary γ' precipitates in a multimodal γ' size distribution RR 1000 alloy to be 15–16 at.pct compared to approximately 12 at.pct in the secondary γ' precipitates.⁵ Goodfellow *et al.* experimentally demonstrated that the partitioning of Mo to the γ phase increased the γ lattice parameter by approximately 0.03Å when 5 at.pct Mo was added to Ni–14Cr–5Al–5Ti at.pct,⁴² and ThermoCalc software predicted an even larger change in the lattice parameter associated with the Mo addition. Given that Chen *et al.* demonstrated the Al content can be as much as 4 at.pct higher in tertiary γ' than secondary in RR 1000 and Goodfellow *et al.* demonstrated that small changes in chemistry can shift the lattice parameter sufficiently to alter the sign of the misfit, it is our belief based on this literature that compositional differences between the precipitate size distributions result in the different γ' lattice parameters and misfit sign at 750 °C [Figure 5(a)].

It has previously been stated that coarsening is restricted by low misfit values.⁴³ But more recently, Meher *et al.* concluded the opposite that low interfacial energies and lattice misfits alone do not impart significantly improved γ' coarsening resistance, presumably as elemental diffusivity is a critical rate controlling parameter.⁴⁴ However, as discussed above, it is clear that a large lattice parameter misfit does have a significant

influence on the transient coarsening regime due to precipitate splitting.

Pollock and Argon^{45,46} suggested that a negative lattice parameter misfit value enhances tensile creep properties in high-volume fraction single crystal superalloys, and in general, single crystal turbine blade alloys possess a negative lattice parameter misfit (which can be inferred from precipitate raft orientation.⁴⁷) Tertiary γ' has been shown to increase creep resistance^{48–50} by hindering the glide of $a/2 < 110gt$ perfect matrix dislocations between the secondary γ' precipitates. Based on the theory of Pollock and Argon, it can be suggested that strengthening of tertiary γ' is also attributed to a local compressive strain in the γ channels.^{45,46} Creep tests of Ni 115 between 700 and 800 °C have previously been interpreted with the aid of a physically based creep model and suggested that fine γ' influences the dislocation motion.⁴⁶ The *in situ* results herein support that tertiary γ' goes rapidly into dissolution at the upper temperature of the creep tests previously published (800 °C). Further research is needed in this field to conclude the role of nanoscale γ' precipitates on high temperature mechanical properties.

The microhardness decreases from 580 °C to the lowest recorded value of 460 Hv at 950 °C, Figure 8(d). This is coupled with a decrease in precipitate area fraction [Figure 8(a)] and a loss of coherency between secondary γ' precipitates and matrix, where $\delta = 0.70 \text{ pct}$ at 950 °C. Both of these microstructural evolutions are suggested to contribute to the loss in hardness, based on the following discussion.

The fixed line tension model, derived from the energy per unit length of dislocation, can be used to estimate the critical shear stress for Orowan bowing^{51–53}

$$\tau(\text{bow}) = Gb/L \quad [1]$$

where G is the shear modulus, b is the Burgers vector, $L = \lambda + 2\bar{R}$, λ is the mean inter-particle, and \bar{R} is the mean particle radius. The inter-particle distance is approximated as the square lattice distance between two spheres in a system where all particles have radius $R = \bar{R}^4$

$$\lambda = 1.6\bar{R}[(\pi/4V)^{0.5} - 1] \quad [2]$$

and V is the precipitate area fraction. For precipitate shear by weakly coupled dislocations, where the dislocation pair is never simultaneously within the same precipitate, Brown and Ham derive an expression for the shear stress required for a dislocation pair to cut a particle⁵³

$$\tau_{(\text{cut,weak})} = \frac{\gamma}{2b} \left[\left(\frac{8\gamma V \bar{R}}{\pi G b^2} \right)^{0.5} - V \right] \quad [3]$$

where γ is the antiphase boundary energy. For precipitate shear by strongly coupled dislocations, where the dislocation pair is simultaneously shearing the same precipitate, the particle shear stress can be expressed as^{43,54–56}

$$\tau(\text{cut}, \text{strong}) = \left(\frac{3}{2}\right)^{0.5} V^{0.5} G b \left(\frac{2\pi\gamma\bar{R}}{Gb^2} - 1\right)^{0.5} \quad [4]$$

These calculations are performed and presented in Table II as an approximation for the relative change in shear strength due to the decrease in precipitate volume fraction between 900 and 950 °C. G is approximated from CMSX-4 data due to a lack of data for Ni 115.⁴⁶ The (111) plane antiphase boundary energy for the Ni 115 composition (Table I) is calculated at 900 and 950 °C using thermodynamic calculations^{57,58} with Open CALPHAD,⁵⁹ implemented in Materials Square software.⁶⁰

It is clear that these analytical expressions do not quantitatively predict superalloy strength; however, they can be applied for qualitative guidance. The equations infer that yield occurs via Orowan bowing or shear of the secondary γ' precipitates by strongly coupled dislocations at 900 °C. Generally, only the bowing mechanism operates in incoherent particle strengthened systems,⁶¹ and the associated decrease in yield strength is estimated to be 7.5 based on the Orowan bowing calculations and the loss of precipitate coherency.

Goodfellow *et al.*⁸ attempted to separate the relative contributions of strengthening mechanisms to overall strength and estimated that coherency strains provide approximately 5 pct of total yield strength in RR1000. This is of a similar magnitude to the decrease in strength derived above regarding the decrease in area fraction, and thus, the authors' believe that both the loss of coherency and precipitate fraction are both significant to the ~ 950 °C 6–10 pct overall hardness decrease following the 950 °C thermal exposure.

It was previously noted that the lattice response to changes in temperature is very different in the (110) to the (100), Figure 7. The lattice parameters calculated from the (110) and (100) diffraction peaks are approximately equal on temperature steps to 900 and 950 °C, as expected and providing confidence in our methodology. The unequal lattice parameters calculated at lower temperatures may be attributed to intergranular residual strains within the alloy from the prior forging process.

Table II. Analytical Solutions for the Critical Resolved Shear Stress for Deformation to Occur via Dislocation Bowing or Weakly or Strongly Coupled Dislocation Precipitate Shear at Two Different Volume Fractions of Precipitate

T (°C)	900	950
G (GPa)	35	35
b (Å)	2.54	2.54
\bar{R} (nm)	100	100
V (°)	0.58	0.48
γ (J/m ²)	0.294	0.292
λ (nm)	26	45
$\tau(\text{bow})$ (MPa)	39	36 (– 7.5 pct)
$\tau(\text{cut}, \text{weak})$ (MPa)	2209	2019 (– 8.7 pct)
$\tau(\text{cut}, \text{strong})$ (MPa)	134	121 (– 9.3 pct)

It is unclear why the lattice parameter in the (110) initially decreases 750 to 800 °C, while the (100) increases, Figure 7. It is not intuitive that such anisotropic behavior would be related to dissolution of γ' . Shrinkage during service of specific superalloys and the underlying mechanisms have been discussed in several studies^{62–64} and are often associated with short range ordering of Ni₂Cr and the transformation into long range ordering under long-term aging. Cadel *et al.* have noted cluster formation within γ' with stoichiometry close to that of Ni₂Cr in superalloy N18, an alloy which possesses 12.3 at.pct (11.4 wt.pct) Cr in the bulk composition, despite being treated at temperatures well above the critical order–disorder temperature of this phase ($T_c = 590$ °C for binary Ni₂Cr).⁶⁵ It is possible that the presence of additional alloying elements could increase the critical temperature.⁶⁵ Metcalfe and Nath⁶⁴ used the (331) diffraction peak position to conclude that Ni₂Cr ordering in Nimonic 80A causes lattice contraction within the temperatures studied (up to 600 °C).

Gwalani *et al.* examined the ordering–disordering transformation in Ni-33 at.pct Cr and noted that disordering occurred between 620 °C – 750 °C, inferred from a non-linear lattice expansion coefficient.⁶⁶ To our knowledge, the data analysis presented herein is the first to analyze the (110) and (100) peaks separately and observe an anisotropic lattice response at temperature. The (100) of the orthorhombic structure Ni₂Cr phase is parallel to the (110) axes of the fcc and L1₂ phases; thus, any disordering could be observed in the (110) γ' reflection. Additionally, direct observation of such localized clustering or short range ordering and disordering would be inherently difficult to directly observe by experimentation. The authors are of the opinion that the anisotropy is associated with intergranular effects and not local anisotropy in the cubic structure. This residual strain is relieved as the heat treatments increase above 800 °C, which also corresponds with the tertiary γ' dissolution.

V. CONCLUSIONS

In conclusion, thermally induced microstructure evolution of the multimodal γ' nickel superalloy has been examined between 750 and 950 °C temperature holds by a multi-technique analysis. Precipitate splitting is shown to be a dominant particle evolution mechanism in the transient coarsening regime and related to the large lattice parameter misfit of the alloy. The lattice parameters of secondary and tertiary γ' differ and result in non-symmetric γ' diffraction peaks which can be deconvoluted to extract microstructural parameters of both size distributions. The tertiary γ' precipitates go into dissolution at 800 °C according to SEM, and there is a corresponding change in diffraction peak shape, supporting our conclusion that both size distributions can be observed and separated by diffraction analysis. The lattice parameter misfit is positive for the secondary γ'

precipitates but negative for the tertiary γ' precipitates which will alter the local strain field and enhance material properties according to Pollock and Argon.⁴⁵ Both precipitate splitting and dissolution of tertiary γ' precipitates do not have an observable effect on microhardness values; however, the loss of coherency and reduction of secondary γ' precipitate volume fraction above 900 °C decreases microhardness. There appears to be intergranular residual strains in the sample, where the lattice parameters calculated from the (100) and (110) are not equal. It is suggested that this strain may be residual from the forging process. The lower-temperature heat treatments do not relieve this residual strain. Above 800 °C, following dissolution of the tertiary γ' and with increased diffusivity, the residual strain is relieved.

ACKNOWLEDGMENTS

We are grateful for the assistance and support of Dr. Chip Tomonto and Dr. Colton Steiner in facilitating our research at The UM College of Engineering—Johnson & Johnson 3D Printing Center of Excellence Collaborative Laboratory. This research used the resources of the Advanced Photon Source, a US Department of Energy (DOE) Office of Science User Facility, operated for the DOE Office of Science by Argonne National Laboratory under Contract No. DE-AC02-06CH11357.

CONFLICT OF INTEREST

On behalf of all authors, the corresponding author states that there is no conflict of interest.

REFERENCES

1. F. Schulz, H.Y. Li, H. Kitaguchi, D. Child, S. Williams, and P. Bowen: *Metall. Mater. Trans. A* 2018, vol. 49, pp. 3874–84.
2. S.T. Wlodek, M. Kelly, and D.A. Alden: *Superalloys* 1996, vol. 129–136, p. 1996.
3. M. Li, J. Coakley, D. Isheim, G. Tian, and B. Shollock: *J. Alloys Compds.* 2018, vol. 732, pp. 765–76.
4. J. Coakley, H. Basoalto, and D. Dye: *Acta Mater.* 2010, vol. 58, pp. 4019–4028.
5. Y.Q. Chen, E. Francis, J. Robson, M. Preuss, and S.J. Haigh: *Acta Mater.* 2015, vol. 85, pp. 199–206.
6. M. Zhang, G. Liu, H. Wang, and H. BenFu: *Sci. China Technol. Sci.* 2018, vol. 61, pp. 1824–28.
7. H.Y. Li, J.F. Sun, M.C. Hardy, H.E. Evans, S.J. Williams, T.J.A. Doel, and P. Bowen: *Acta Mater.* 2015, vol. 90, pp. 355–369.
8. A.J. Goodfellow, E.I. Galindo-Nava, C. Schwalbe, and H.J. Stone: *Mater. Des.* 2019, vol. 173, pp. 107760.
9. D.M. Collins and H.J. Stone: *Int. J. Plast.* 2014, vol. 54, pp. 96–112.
10. G. Bruno, B. Schönfeld, and G. Kostorz: *Int. J. Mater. Res.* 2003, vol. 94, pp. 12–18.
11. G. Bruno, G. Schumacher, H.C. Pinto, and C. Schulze: *Metall. Mater. Trans. A* 2003, vol. 34, pp. 193–197.
12. H.C. Pinto and G. Bruno: *J. Synchrotron Radiat.* 2003, vol. 10, pp. 148–53.
13. G. Bruno, B. Schönfeld, G. Kostorz: *Int. J. Mater. Res.* 2003, vol. 94, pp. 12–18.
14. G. Bruno, H. C. Pinto: The kinetics of the γ' phase and its strain in the nickel base superalloy sc16 studied by *in-situ* neutron and synchrotron radiation diffraction. In *Proceedings of the 10th International Symposium on Superalloys (SUPERALLOYS'04)*, pp. 837–46.
15. D.M. Collins, L. Yan, E.A. Marquis, L.D. Connor, J.J. Ciardiello, A.D. Evans, and H.J. Stone: *Acta Mater.* 2013, vol. 61, pp. 7791–804.
16. S. Neumeier, F. Pyczak and M. Göken: *Mater. Des.* vol. 198, p. 109362.
17. F. Pyczak, B. Devrient and H. Mughrabi: *Superalloys* 2004, vol. 827–836, p. 2004.
18. F. Pyczak, B. Devrient, F. C. Neuner, and H. Mughrabi: *Acta Mater.*, vol. 53, pp. 3879–3891.
19. M. Preuss, J.Q. da Fonseca, B. Grant, E. Knoche, R. Moat, and M. Daymond: *Superalloys* 2008, vol. 11, pp. 405–414.
20. Y. Lu, S. Ma, and B.S. Majumdar: *Superalloys*, 2008, vol. 553.
21. D. Dye, J. Coakley, V.A. Vorontsov, H.J. Stone, and R.B. Rogge: *Scr. Mater.* 2009, vol. 61, pp. 109–112.
22. J. Coakley, R.C. Reed, J.L.W. Warwick, K.M. Rahman, and D. Dye: *Acta Mater.* 2012, vol. 60, pp. 2729–38.
23. J. Coakley, and D. Dye: *Scr. Mater.* 2012, vol. 67, pp. 435–38.
24. J. Coakley, E.A. Lass, D. Ma, M. Frost, D.N. Seidman, D.C. Dunand and H.J. Stone. *Scr.Mater.*, 2017, vol. 134, pp. 110–14.
25. J. Coakley, D. Ma, M. Frost, D. Dye, D.N. Seidman, D.C. Dunand, and H.J. Stone: *Acta Mater.*, 135: 77–87 (2017).
26. J. Coakley, E.A. Lass, D. Ma, M. Frost, H.J. Stone, D.N. Seidman, D.C. Dunand: *Acta Mater.*, 2017, vol. 136, pp. 118–25.
27. H.J. Stone, T.M. Holden, R.C. Reed, *Acta Mater.* 1999, vol. 47, pp. 4435–4448.
28. D. Dye, H.J. Stone, R.C. Reed, *Curr. Opin. Solid State Mater. Sci.* 2001, vol. 5, pp. 31–37.
29. H.J. Stone, R.C. Reed, T.M. Holden: *Scri. Mater.*, 1999, vol. 40.
30. D. Shahriari, M.H. Sadeghi, A. Akbarzadeh, and M. Cheraghzadeh: *Int. J. Adv. Manuf. Technol.* 2009, vol. 45, pp. 841–50.
31. A. Jain, S.P. Ong, G. Hautier, W. Chen, W.D. Richards, S. Dacek, S. Cholia, D. Gunter, D. Skinner, G. Ceder, K.A. Persson. *APL Mater.* 2013, vol. 1, p. 011002.
32. Y. Chen, T.J.A. Slater, M. Bai, R. Mitchell, O. Ciuca, M. Preuss and S.J. Haigh, et al.: *Acta Mater.*, 2016, vol. 110, pp. 295–305.
33. A. Hazotte, T. Grosdidier and S. Denis: *Scr. Mater.*, 1996, vol. 34.
34. M. Doi: *Mater. Trans.* 1992, vol. 33, pp. 637–49.
35. B. Wahlmann, F. Galgon, A. Stark, S. Gayer, N. Schell, P. Staron, and C. Koerner: *Acta Mater.* 2019, vol. 180, pp. 84–96.
36. Y. Chen, R. P. Babu, T. Slater, R. Mitchell, O. Ciuca, and M. Preuss: On the diffusion-mediated cyclic coarsening and reversal coarsening in an advanced ni-based superalloy. In *European Microscopy Congress 2016: Proceedings*, 2016, pp. 281–82. Wiley Online Library.
37. A.J. Goodfellow, E.I. Galindo-Nava, K.A. Christofidou, N.G. Jones, T. Martin, P.A.J. Bagot, C.D. Boyer, M.C. Hardy, and H.J. Stone. *Metall. Mater. Trans. A* 2018, vol. 49, pp. 718–28.
38. W. Yuting, C. Li, X. Xia, H. Liang, Q. Qi, Y. Liu: *J. Mater. Sci. Technol.* 2021, vol. 67, pp. 95–104.
39. W. Xia, X. Zhao, L. Yue, and Z. Zhang: *J. Alloys Compds.* 2020, vol. 819, p. 152954.
40. C. Wagner: *Z. Elektrochem* 1961, vol. 65, pp. 581–91.
41. I.M. Lifshitz and V.V. Slyozov: *J. Phys. Chem. Solids*, 1961, vol. 19, pp. 35–50.
42. A.J. Goodfellow, L.R. Owen, K.A. Christofidou, J. Kelleher, M.C. Hardy, and H.J. Stone: *Metals* 2019, vol. 9, p. 700.
43. R.C. Reed: *The Superalloys: Fundamentals and Applications*. Cambridge University Press, 2008.
44. S. Meher, M.C. Carroll, T.M. Pollock, L.J. Carroll: *Mater. Des.* 2018, vol. 140, pp. 249–56.
45. T.M. Pollock and A.S. Argon: *Acta Metall Mater* 1992, vol. 40, pp. 1–30.
46. J. Coakley: *Creep and Microstructure Evolution in Nickel Superalloys*. PhD Thesis, Imperial College London 2010.
47. H. Mughrabi: *Acta Mater.* 2018, vol. 81, pp. 21–29.
48. K. Kakehi: *Metall. Mater. Trans. A* 1999, vol. 30, pp. 1249–59.
49. J.-B. Le Graverend, J. Cormier, M. Jouiad, F. Gallerneau, P. Paulmier, and F. Hamon: *Mater. Sci. Eng. A* 2010, vol. 527, pp. 5295–302.

50. D. Locq, P. Caron, S. Raujol, F. Pettinari-Sturmel, A. Coujou, and N. Clément: *Superalloys* vol. 2004, pp. 179–87.
51. J. Friedel: *Dislocations: International Series of Monographs on Solid State Physics*, volume 3. Elsevier 2013.
52. A.H. Cottrell: *Am. J. Phys.* 1954, vol. 22, pp. 242–43.
53. L.M. Brown and R.K. Ham: Dislocation-particle interactions. *Strengthening Methods in Crystals*, 1971, pp. 9–135.
54. W. Hühner and B. Reppich: *Int. J. Mater. Res.* 1978, vol. 69, pp. 628–34.
55. D. Hull and D.J. Bacon: *Introduction to Dislocations*. Butterworth-Heinemann, 2001.
56. M.P. Jackson and R.C. Reed: *Mater. Sci. Eng. A* 1999, vol. 259, pp. 85–97.
57. M. Chandran and S.K. Sondhi: *Modell. Simul. Mater. Sci. Eng.* 2011, vol. 19, 025008.
58. A.P. Miodownik and N. Saunders: The calculation of apb energies in 112 compounds using a thermodynamic database. *Applications of Thermodynamics in the Synthesis and Processing of Materials*, P. Nash and B. Sundman (eds.) (Warrendale, PA: TMS, 1995), vol. 91, 1995.
59. B. Sundman, U.R. Kattner, M. Palumbo, and S.G. Fries: *Integrat. Mater. Manuf. Innov.*, 2015, vol. 4, pp. 1–15.
60. Virtual Lab. Inc: materials square. 2017. <https://www.materialsquare.com/>.
61. R.R. Jensen and J.K. Tien: *Metall. Trans. A*, 1985, vol. 16, pp. 1049–68.
62. J. Moverare: Shrinkage and ageing of ni-base alloys at intermediate temperatures (400–600°C). finspång: Siemens industrial turbomachinery ab. Technical Report, Internal technical report 1CS51497 2005.
63. A. Marucco and B. Nath: *J. Mater. Sci.* 1988, vol. 23, pp. 2107–14.
64. E. Metcalfe, B. Nath, and A. Wickens: *Mater. Sci. Eng.*, 1984, vol. 67, pp. 157–62.
65. E. Cadel, D. Lemarchand, S. Chambrelaud, and D. Blavette: *Acta Mater.* 2002, vol. 50, pp. 957–66.
66. B. Gwalani, T. Alam, C. Miller, T. Rojhirunsakool, Y.S. Kim, S.S. Kim, M.J. Kaufman, Y. Ren, and R. Banerjee. *Acta Mater.*, 2016, 115: 372–84.

Publisher's Note Springer Nature remains neutral with regard to jurisdictional claims in published maps and institutional affiliations.

Springer Nature or its licensor (e.g. a society or other partner) holds exclusive rights to this article under a publishing agreement with the author(s) or other rightsholder(s); author self-archiving of the accepted manuscript version of this article is solely governed by the terms of such publishing agreement and applicable law.